

## The Effects of a Mountain on the Propagation of a Preexisting Convective System for Blocked and Unblocked Flow Regimes

HEATHER DAWN REEVES AND YUH-LANG LIN

*Department of Marine, Earth, and Atmospheric Sciences, North Carolina State University, Raleigh, North Carolina*

(Manuscript received 15 February 2006, in final form 3 October 2006)

### ABSTRACT

Observations and previous research of squall lines impinging on mountain ranges have revealed that the squall lines sometimes stall upstream of the mountains for several hours leading to copious accumulations of precipitation. It has been hypothesized that squall-line stagnation may be more prone to occur in flows where the Froude number ( $F = U/Nh$ , where  $U$  is the basic-state wind,  $N$  is the Brunt–Väisälä frequency, and  $h$  is the mountain height) is low. This hypothesis is tested herein through a series of idealized, two-dimensional experiments where a convective system was triggered upstream of a mesoscale mountain in conditionally unstable flow. For simulations with relatively low Froude numbers, stagnation of the preexisting convective system was not observed. In the simulations with high values of  $F$ , squall lines were noted to stagnate between 100 and 200 km upstream of the mountain. This result indicates that squall-line stagnation may be more favored for moderate to large values of  $F$  for conditionally unstable flow. The mechanisms leading to the formation of the stationary convective system upstream of the mountain in the unblocked flows were explored and it was found that evaporative cooling played a pivotal role in the stagnation of the squall line.

### 1. Introduction

Moist flow impinging on steep mountains can cause heavy precipitation and flash flooding. This, in turn, can lead to property damage and loss of life. Observational evidence suggests that these heavy precipitation events typically have an upstream profile with relatively strong winds and low static stability (Caracena et al. 1979; Overland and Bond 1995; Medina and Houze 2003; Galewsky and Sobel 2005). These meteorological characteristics are represented in a nondimensional control parameter called the Froude number ( $F$ ), which is given by

$$F = \frac{U}{Nh}, \quad (1)$$

where  $U$  is the basic-state wind speed,  $N$  is the Brunt–Väisälä frequency, and  $h$  is the mountain height.

In their idealized simulations of moist flow impinging on orography with different values of  $F$ , Chu and Lin

(2000) noted there were three flow regimes analogous to the subcritical, critical, and supercritical flow regimes found in the two-dimensional, shallow-water system. Regime I, the blocked or low  $F$  regime, is characterized by an upstream-propagating density current and convective system. Precipitation accumulations in this regime were found to be modest and evenly distributed upstream of the mountain. Regime II represents a transition from blocked to unblocked flow. In this regime, the propagation speed of the upstream, convection-induced density current is approximately balanced by the basic-state wind. Hence, this regime is characterized by a stationary density current along the peak or upslope of the terrain and modest to high precipitation accumulations over the mountain peak. In regime III, the flow is unblocked and the values of  $F$  are high. The convection-induced density currents in this regime are swept downstream by the relatively strong basic-state wind. Because the flow in this regime is approximately linear, the vertical velocity along the upstream side of the mountain and, consequently, the precipitation, increases with increasing  $U$  leading to large precipitation accumulations on the peak or upslope of the terrain. Additional idealized studies of moist airstreams impinging on orography support the hypothesis that the

---

*Corresponding author address:* H. D. Reeves, Dept. of Marine, Earth, and Atmospheric Sciences, North Carolina State University, 1125 Jordan Hall, Faucette Dr., Raleigh, NC 27695-8208.  
E-mail: hdreeves@unity.ncsu.edu

precipitation distribution does depend on  $F$  with greater accumulations on the mountain peak and upslope being associated with larger values of  $F$  (Jiang 2003; Miglietta and Buzzi 2004; Chen and Lin 2005a,b).

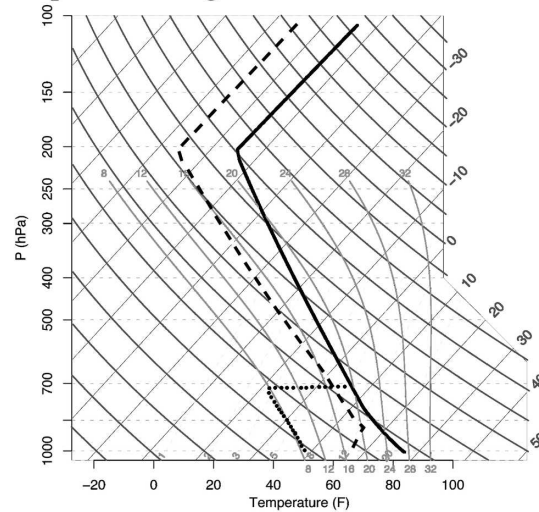
Although there is a large body of work investigating the typical conditions present during cases of heavy, orographically induced precipitation, the effects of a mountain on preexisting convective systems is relatively unexplored. Among the few papers in the literature addressing this subject are those of Akaeda et al. (1995) and Chen et al. (1991) who noted that in some cases of squall lines impinging on the Central Mountain Range (CMR) of Taiwan during the Taiwan Area Mesoscale Experiment (TAMEX; Kuo and Chen 1990), the convective systems appeared to stagnate for several hours upstream of the CMR leading to high precipitation accumulations. In other cases during TAMEX, the convective systems traversed over the mountain range with little or no change in the forward speed of the system and were associated with more modest and even precipitation distributions (Chen and Chou 1993). Akaeda et al. (1995) suggested that the movement of these preexisting squall lines over the orography may have been dictated by the Froude number of the basic-state flow. A similar conclusion was reached by Chen et al. (1991) who noted that during the intensive observation period (IOP-8) of TAMEX, a case of squall-line stagnation,  $F$  was fairly low. Additionally, Wang et al. (2000) noted the behavior of preexisting precipitation systems impinging on the volcanoes of Hawaii appeared to be dependent on the Froude number of the basic-state flow.

Frame and Markowski (2006) considered an idealized case of a squall line embedded in a sheared flow impinging on a mountain. Although the mountain height was varied in their research, the values chosen (between 300 and 900 m) yield relatively high layer-averaged Froude numbers. Their Fig. 3, which shows fields of perturbation  $u$  wind and vertical velocity, indicates that for the 900-m high mountain, the flow was consistent with an unblocked, or high  $F$ , flow. The aim of this paper is to conduct a systematic study investigating the effects of a mountain on a preexisting convective system for both blocked and unblocked flow regimes to see if the hypothesis of Chen et al. (1991) and Akaeda et al. (1995) is true. This paper is organized as follows. The experimental design is presented in section 2. Results from the experiments are discussed in sections 3, 4, and 5. The conclusions are presented in section 6.

## 2. Experimental design

Simulations were performed using the Advanced Regional Prediction System (ARPS) version 5.1.0 (Xue et

### a) input sounding



### b) initial potential temperature profile

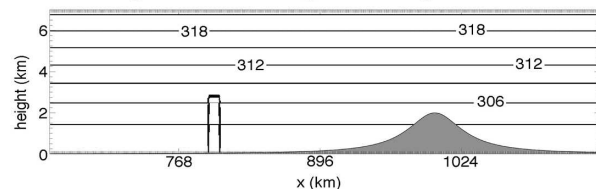


FIG. 1. (a) Sounding used to initialize simulations (after Weisman and Klemp 1982). The dotted line represents the sounding through the temperature perturbation used to trigger the convection. (b) Initial potential temperature distribution of simulations.

al. 2001). This model solves the fully compressible, three-dimensional, nonhydrostatic equations. Terrain-following height coordinates were used in these simulations. Fourth- and second-order advection schemes were used in the horizontal and vertical directions, respectively. The boundary conditions in the east and west directions were radiative. A periodic boundary condition was used for the north and south boundaries. The lower boundary was free slip. Microphysical processes were handled using a parameterization scheme based on Lin et al. (1983). The horizontal grid spacing is 1 km and the horizontal domain has 2000 grid points in the east–west direction. The vertical grid spacing is stretched from 50 m at the surface to  $\sim 400$  m at the domain top. There are 80 vertical levels, which gives a domain height of 19.5 km. A sponge layer was applied above 14 km to reduce artificial wave reflection by the upper boundary. In all simulations, the model time step was 3 s and each simulation was integrated for 12 h. The initial conditions were horizontally homogeneous based on the Weisman–Klemp (1982) sounding (Fig. 1a). This sounding has been chosen because it was used in pre-

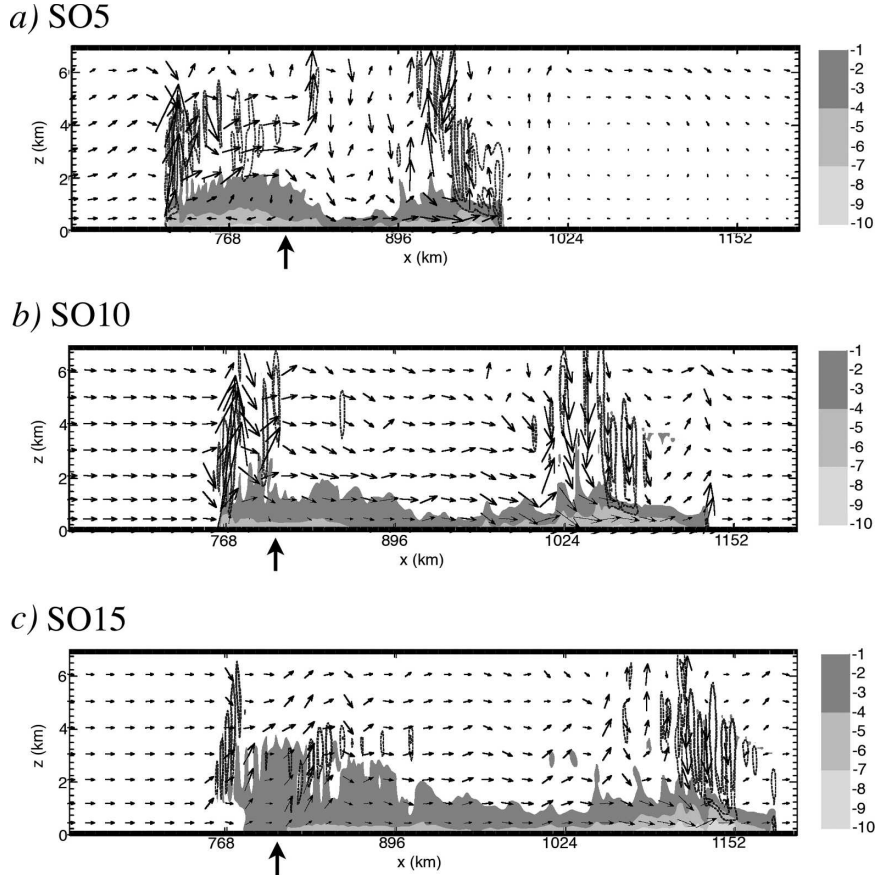


FIG. 2. Vertical cross sections of perturbation potential temperature (shaded as in legend), cloud water mixing ratio (dotted contours; contoured every  $0.5 \text{ g kg}^{-1}$ ), and wind vectors at  $t = 4 \text{ h}$  for the (a) SO5, (b) SO10, and (c) SO15 simulations. The thick arrow beneath each panel indicates the location of the initial cold pool used to force convection.

vious studies of idealized flow over orography (Chu and Lin 2000; Frame and Markowski 2006) to which this study is closely related and its use facilitates a more direct comparison between this study and the above-mentioned papers.

The mountain geometry is given by

$$h(x) = \frac{h_m a^2}{a^2 + (x - x_0)^2}, \quad (2)$$

where  $h(x)$  is the terrain height function,  $h_m$  is the maximum terrain height (2000 m),  $a$  is the half-width (30 km), and  $x_0$  is the location of the mountain peak (1000 km from the left boundary). The mountain was introduced impulsively into the domain at  $t = 0 \text{ s}$ .

The preexisting convective system was triggered by a surface cold perturbation situated 200 km upstream of the mountain (i.e., 800 km from the left boundary). The cold potential temperature perturbation, which was 18 K colder than the surroundings, was rectangular in

shape with a height of 2800 m and a width of 10 km. Cooling was imposed only at  $t = 0 \text{ s}$ . The initial potential temperature field for the simulations is shown in Fig. 1b.

Three sets of experiments were performed. The first set of simulations was designed to assess the manner in which the convective system alone alters the flow field. In these experiments, there was an initial cold pool, but no mountain. The second set of simulations was designed to assess how the orography alone alters the flow field, so only a mountain was included in these experiments, (i.e., there was no initial cold pool). In the third set of experiments, both the cold pool and the mountain were included in order to determine the combined effects of these two forcings. In all three sets of experiments, simulations were conducted wherein the basic-state wind,  $U$ , was varied from 1 to  $20 \text{ m s}^{-1}$  in  $1 \text{ m s}^{-1}$  increments. We will use the following nomenclature for the simulations: the mountain-only simulations will be referred to as MOX, the squall-line-only simulations as

SOX, and the simulations with both the squall line and the mountain as SMX where the  $X$  refers to the basic-state wind speed.

### 3. Experiment results

#### a. Results from the SO simulations

Previous research on idealized, two-dimensional squall lines over flat terrain shows that there are two convection-induced density currents that propagate away from the location of forcing. For relatively low values of  $U$ , the left density current propagates upstream (Liu and Moncrieff 1996) and its leading edge, or nose, is elevated compared to the trailing region of the current (Britter and Simpson 1980). This behavior was noted in our SO simulations with  $U$  wind speeds less than  $10 \text{ m s}^{-1}$ . Figure 2a shows a vertical cross section of perturbation potential temperature ( $\theta'$ ) less than 0 K, cloud water mixing ratio ( $q_c$ ), and wind vectors at  $t = 4 \text{ h}$  for the SO5 simulation. The location of the initial cold pool is given by the thick, solid arrow beneath the panel. Note that the convection-induced density current, which can be identified by the region of  $\theta' < -4 \text{ K}$ , split into two branches with the left branch propagating upstream. Also note that the left density current had an elevated head, as in previous idealized simulations. Convective clouds were present along the leading edge of each density current.

Chu and Lin (2000) found that for a certain critical value  $U = U_c$ , the propagation speed of the left density current is insufficient for it to propagate upstream and, hence, remains stationary at the location of forcing. This happened in our SO simulations for a  $U$  wind speed of  $10 \text{ m s}^{-1}$  as is illustrated in Fig. 2b, which shows the vertical cross section of  $\theta'$ ,  $q_c$ , and wind vectors from the SO10 simulation. Notice that the left density current, which was located at about  $x = 768 \text{ km}$ , had not moved very far from the location of forcing. The wind vectors indicate there was fairly vigorous vertical ascent at the leading edge of this density current. As in the SO5 simulation, the leading edge of each density current in the SO10 simulation was characterized by a convective cloud.

Raymond and Rotunno (1989) demonstrated that when  $U$  is sufficiently large, the left density current is unable to propagate upstream and is advected downstream by the relatively strong basic-state flow. They further noted that the leading edge of the density current may be more tapered, or flattened, compared to those cases where the density current is able to propagate upstream. This was noted for our SO simulations with  $U > 10 \text{ m s}^{-1}$  and is demonstrated in Fig. 2c for the SO15 simulation. Note that along the leading edge of

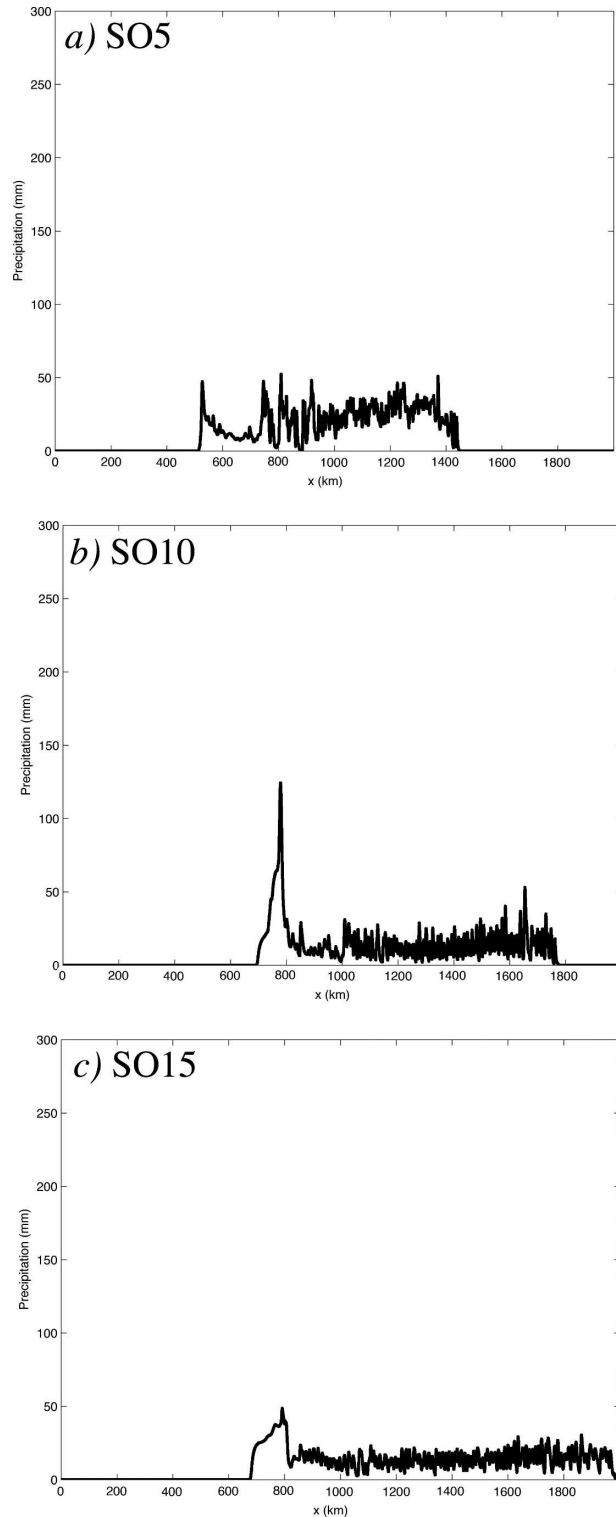


FIG. 3. The 12-h accumulated precipitation for the (a) SO5, (b) SO10, and (c) SO15 simulations.

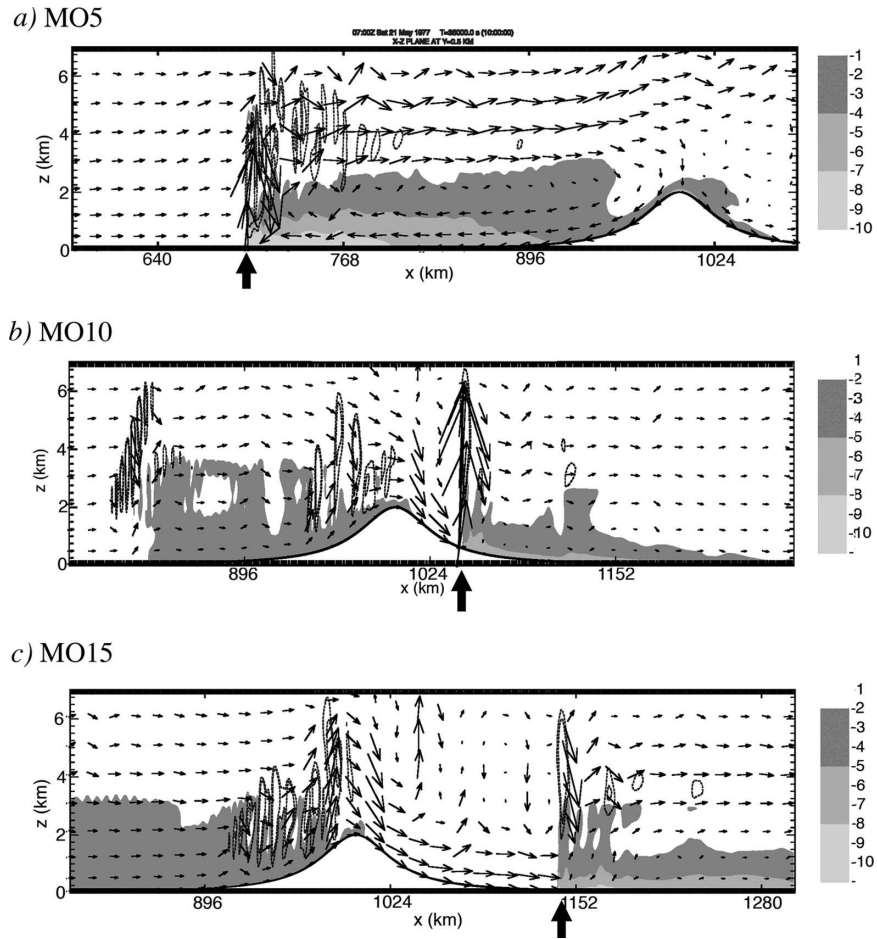


FIG. 4. Vertical cross sections of perturbation potential temperature (shaded as in legend), cloud water mixing ratio (dotted contours; contoured every  $0.5 \text{ g kg}^{-1}$ ), and wind vectors at  $t = 10 \text{ h}$  for the (a) MO5, (b) MO10, and (c) MO15 simulations. The thick arrows indicate the location of the leading edge of the left density current.

the left density current, which at this time was located at about  $x = 816 \text{ km}$ , the vertical velocities were much weaker than in the SO10 case (Fig. 2b). There was a cellular cloud structure along the leading edge of the left density current in Fig. 2c, but it was weaker than that in the SO10 simulation. The cloud system upstream of the left density current, located at approximately  $768 \text{ km}$ , is due to upstream-propagating gravity waves (not shown).

The 12-h accumulated precipitation for the SO5, SO10, and SO15 simulations is given in Fig. 3. According to this figure, the SO5 and SO15 cases (Figs. 3a,c) are characterized by modest precipitation accumulations that are more-or-less evenly distributed. The SO10 case (Fig. 3b) has a precipitation maximum of  $124 \text{ mm}$  located  $780 \text{ km}$  from the upstream boundary. This relatively large maximum is due to the fact that the left density current in this simulation was quasi-stationary.

*b. Results from the MO simulations*

Figure 4 shows vertical cross sections of  $\theta'$ ,  $q_c$ , and wind vectors for the MO5, MO10, and MO15 cases at  $t = 10 \text{ h}$ . The Froude numbers, using the layer between  $z = 0$  and  $2 \text{ km}$ , for the MO5, MO10, and MO15 simulations are  $0.317$ ,  $0.634$ , and  $0.951$ , respectively. An upstream-propagating density current is clearly evident as the region of  $\theta' < -4 \text{ K}$  in the MO5 simulation (Fig. 4a). The thick arrow beneath each panel in Fig. 4 indicates the location of the leading edge of the left density current. Along the leading edge of this density current, there was strong vertical ascent and a convective cloud. This simulation represents flow in regime I (Chu and Lin 2000). As in the SO simulations, the speed of the upstream-propagating density current decreased with increasing  $U$  until a critical state was reached wherein the left density current no longer moved upstream and

the flow transitioned from a blocked to an unblocked flow regime. Figure 4b, which shows the vertical cross section for the MO10 simulation, indicates that this transition occurred at a  $U$  wind speed of  $10 \text{ m s}^{-1}$ . At the time shown in this figure, the left density current was located about halfway down the lee side of the mountain. There was strong vertical ascent along the leading edge of the left density current but relatively modest ascent along the mountain upslope. Convective clouds were present over the upslope and downslope of the mountain at this time. The vertical cross section for the MO15 simulation is shown in Fig. 4c. The left density current can be seen at this time to be positioned about 140 km downstream of the mountain peak. Note that the vertical velocities over the upslope of the mountain in the MO15 simulation were stronger than in the MO10 simulation as were the convective clouds. The MO15 case belongs to regime III. The weak cooling upstream of the mountain and convective clouds positioned far upstream of the mountain in the MO10 and MO15 simulations are due to precipitation associated with upstream-propagating gravity waves (Raymond and Rotunno 1989). Inspection of the thermodynamic characteristics downstream of the gravity waves and upstream of the mountain indicates that the flow properties were not significantly affected by the presence of these waves (not shown).

The 12-h accumulated precipitation, provided in Fig. 5, shows that for the MO5 simulation (Fig. 5a), the precipitation accumulations were more-or-less evenly distributed upstream of the mountain with relatively modest accumulations. In the MO10 and MO15 simulations (Figs. 5b,c), there was a precipitation maximum over the peak of the mountain associated with stationary precipitation systems that formed over the mountain peak and upslope, the magnitude of which increased with increasing  $U$ . Note that in the MO10 simulation (Fig. 5b), this maximum was about 200 mm while in the MO15 simulation (Fig. 5c), the maximum was about 260 mm. Precipitation accumulations associated with the downstream-propagating density currents in the MO5, MO10, and MO15 cases were rather low (between 10 and 25 mm).

### c. Results from the SM simulations

Figure 6a shows a Hovmöller diagram of the rain rate for the SM5 simulation. In this figure, the triggered convective system can be identified as the upstream-propagating precipitation system originating at  $x = 800$  km. A second convective system originated over the mountain upslope. This precipitation system also propagated upstream eventually merging with the triggered

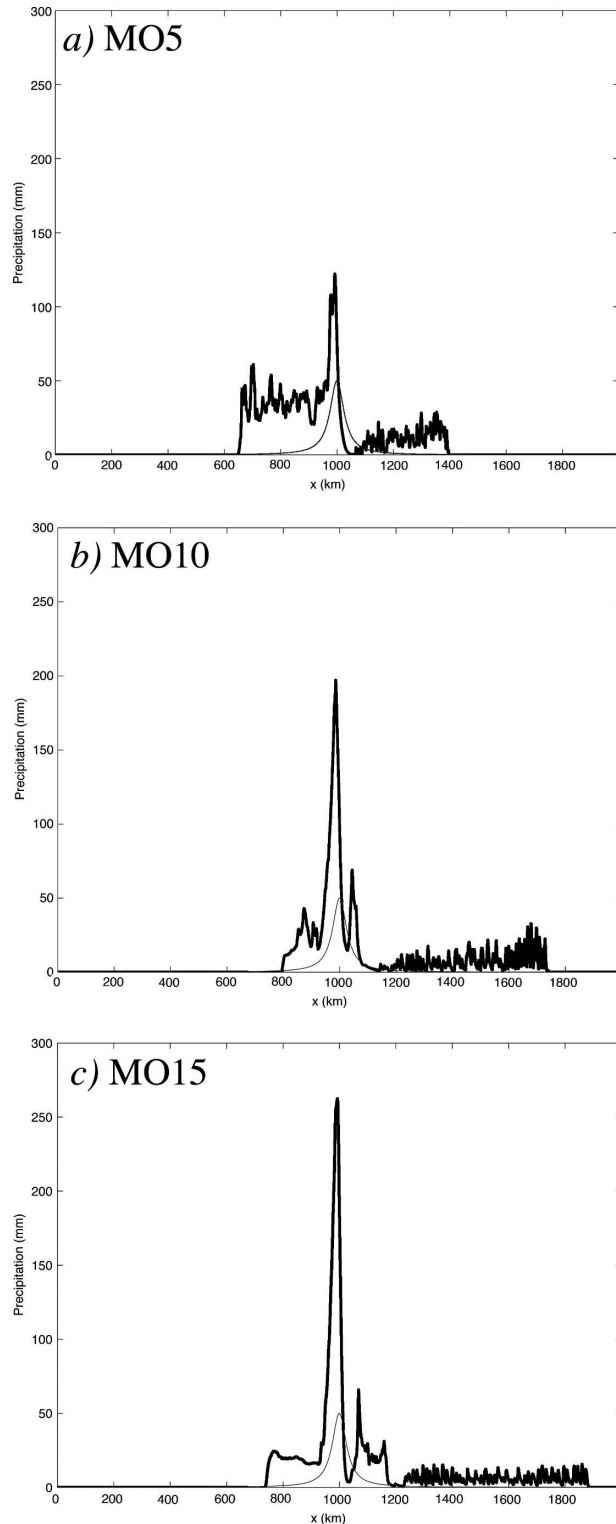


FIG. 5. The 12-h accumulated precipitation for the (a) MO5, (b) MO10, and (c) MO15 simulations.

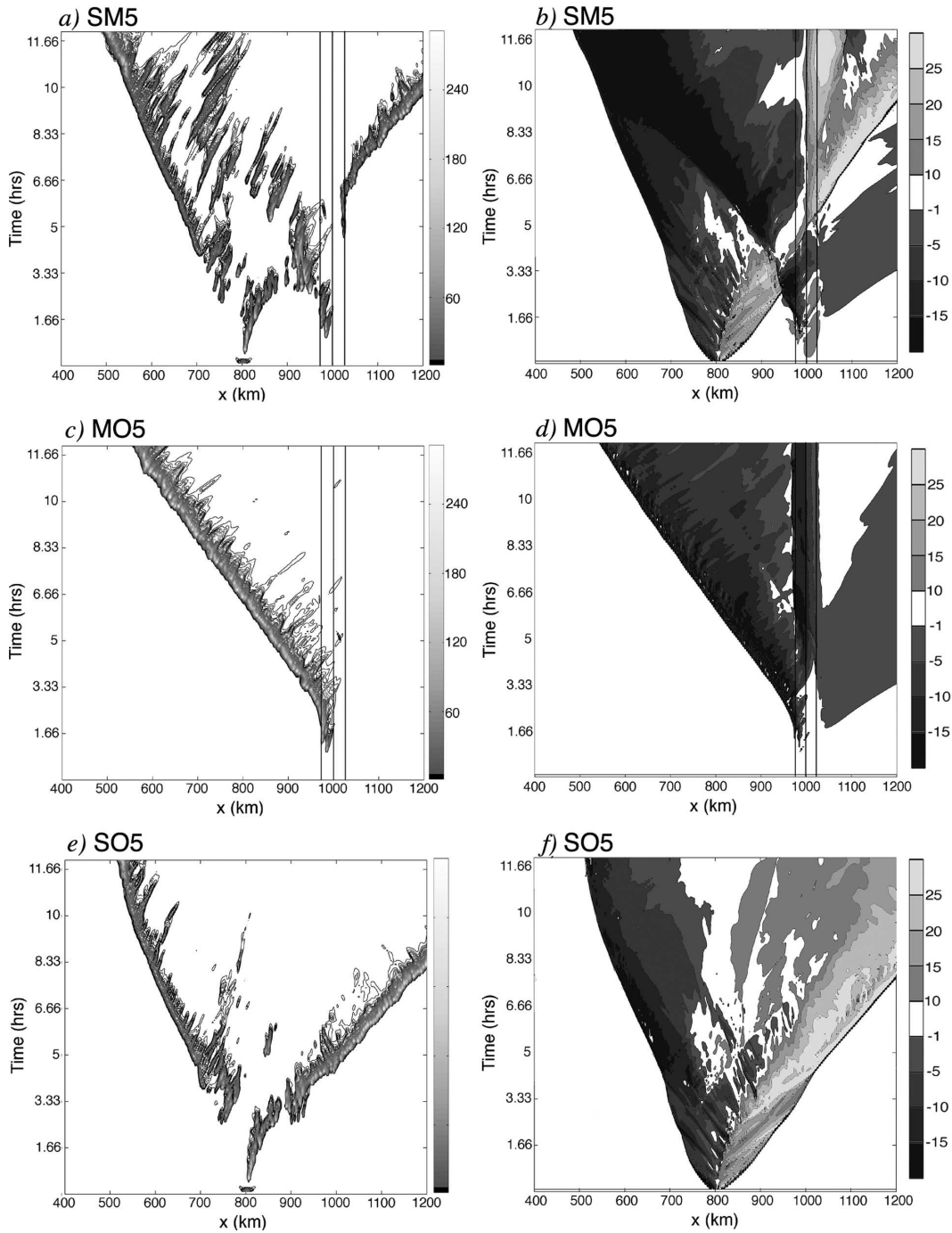


FIG. 6. Hovmöller diagrams of the rain rate for the (a) SM5, (c) MO5, and (e) SO5 simulations and Hovmöller diagrams of surface  $u$  winds for the (b) SM5, (d) MO5, and (f) SO5 simulations. The thin black lines in (a)–(d) denote the mountain peak and half-width.

convective system between  $t = 8$  and 10 h. Rain rates were locally enhanced at the time and location of the merger, but the precipitation system did not become stationary. Also note that there was no long-lived stationary precipitation system upstream of the mountain

at any time during the simulation. A Hovmöller diagram of surface  $u$  winds for the SM5 case is provided in Fig. 6b. In this figure upstream (downstream) propagating density currents can be identified as the region of negative  $u$  (enhanced  $u$ ) winds. The density currents

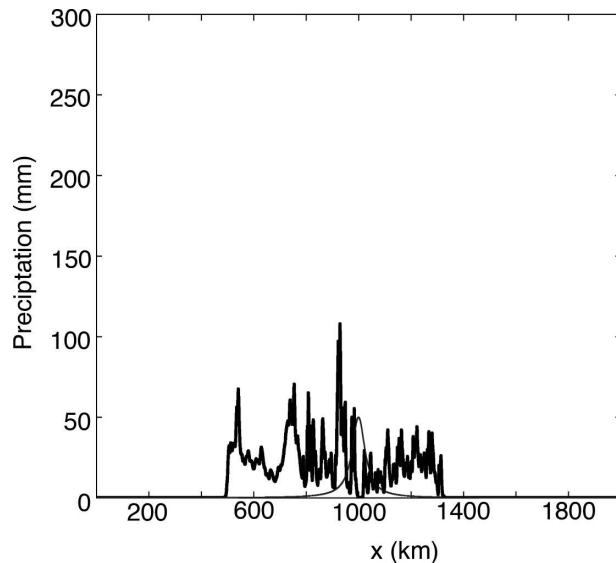


FIG. 7. The 12-h accumulated precipitation for the SM5 simulation.

associated with the triggered convective system and the mountain propagated upstream throughout the duration of the integration period and merged together between  $t = 8$  and 10 h.

Hovmöller diagrams of the rain rate and surface  $u$  winds for the SO5 and MO5 simulations are included in Figs. 6c–f. The upstream-propagating precipitation systems in Figs. 6c,e are clearly evident as are the upstream-propagating density currents in Figs. 6d,f. These features have already been discussed in sections 3a and 3b and the reason for including these analyses is not to further those discussions but to provide a point of reference for understanding how triggered convective system and the orographically induced convective system interact with one another for low  $F$  flows. When Figs. 6a,b are compared with Figs. 6c–f, it appears that the interaction was a linear one. In other words, each feature, more or less, behaved as it would have if the other feature were not present.

The continuous upstream propagation of the convective systems in the SM5 simulation led to precipitation accumulations (Fig. 7) that were fairly evenly distributed. Similar analyses from the other low  $F$  flows (i.e., SM1–SM9) yield similar results in that the density currents and precipitation systems did not become stationary upstream of the mountain. Note that a low Froude number herein is considered to be a Froude number for which the flow in a horizontally homogeneous atmosphere, without the presence of an embedded convective system, is blocked.

Hovmöller diagrams of the rain rate for the SM10, MO10, and SO10 simulations are shown in Figs. 8a,c,e,

respectively. In the SM10 simulation, there was a stationary precipitation system located at  $x = 800$  km. This precipitation system is qualitatively very similar in location and intensity to that in the SO10 simulation (Fig. 8e). There was also a precipitation system over the mountain peak and upslope in the SM10 simulation during the first 5 h of integration. This system appears very similar to the precipitation system over the mountain in the MO10 simulation (Fig. 8c). The narrow, non-convective, upstream-propagating bands of precipitation in Figs. 8a,c,e are due to the upstream-propagating density currents discussed in sections 3a,b. Figures 8b,d,f show Hovmöller diagrams of surface  $u$  winds for the SM10, MO10, and SO10 simulations, respectively. In the SM10 simulation (Fig. 8b), there was a broad region (about 200 km) of negative  $u$  winds upstream of the mountain after about  $t = 5$  h. This feature was not present at all in the MO10 (Fig. 8d) simulation and was significantly narrower in the SO10 (Fig. 8f) simulation, which hints that as the flow transitions from a blocked to an unblocked state, the interaction between the triggered system and the mountain-induced system becomes nonlinear (i.e., the flow fields are not merely a superposition of those in the corresponding MO and SO simulations). The 12-h accumulated precipitation (Fig. 9) shows there was a local precipitation accumulation of 110 mm at  $x = 790$  km as well as a second precipitation maximum over the mountain peak in the SM10 simulation of 100 mm.

Figure 10a shows a Hovmöller diagram of the rain rate for the SM15 simulation. Both the right and left branches of the triggered convective system moved downstream with the left branch becoming stationary at about  $t = 9$  h and  $x = 850$  km. Inspection of similar plots from the other unblocked SM simulations (i.e., SM11–SM20) indicates that *the left branch of the triggered convective system became stationary between 100 and 200 km upstream of the mountain in all unblocked SM simulations*. Also, according to Fig. 10a, the mountain-induced convective system propagated slowly upstream, merging with the left branch of the triggered convective system at about  $t = 4$  h. The Hovmöller diagram of surface  $u$  winds for the SM15 simulation (Fig. 10b) shows that at the time these two convective systems merged, a region of return flow developed upstream of the mountain whose leading edge was collocated with the leading edge of the merged convective system noted in Fig. 10a. Again, Hovmöller diagrams of the rain rate and surface  $u$  winds from the MO15 and SO15 simulations have been included for comparative purposes. And again, one can clearly see that the flow fields in the SM15 simulation are not a linear combina-

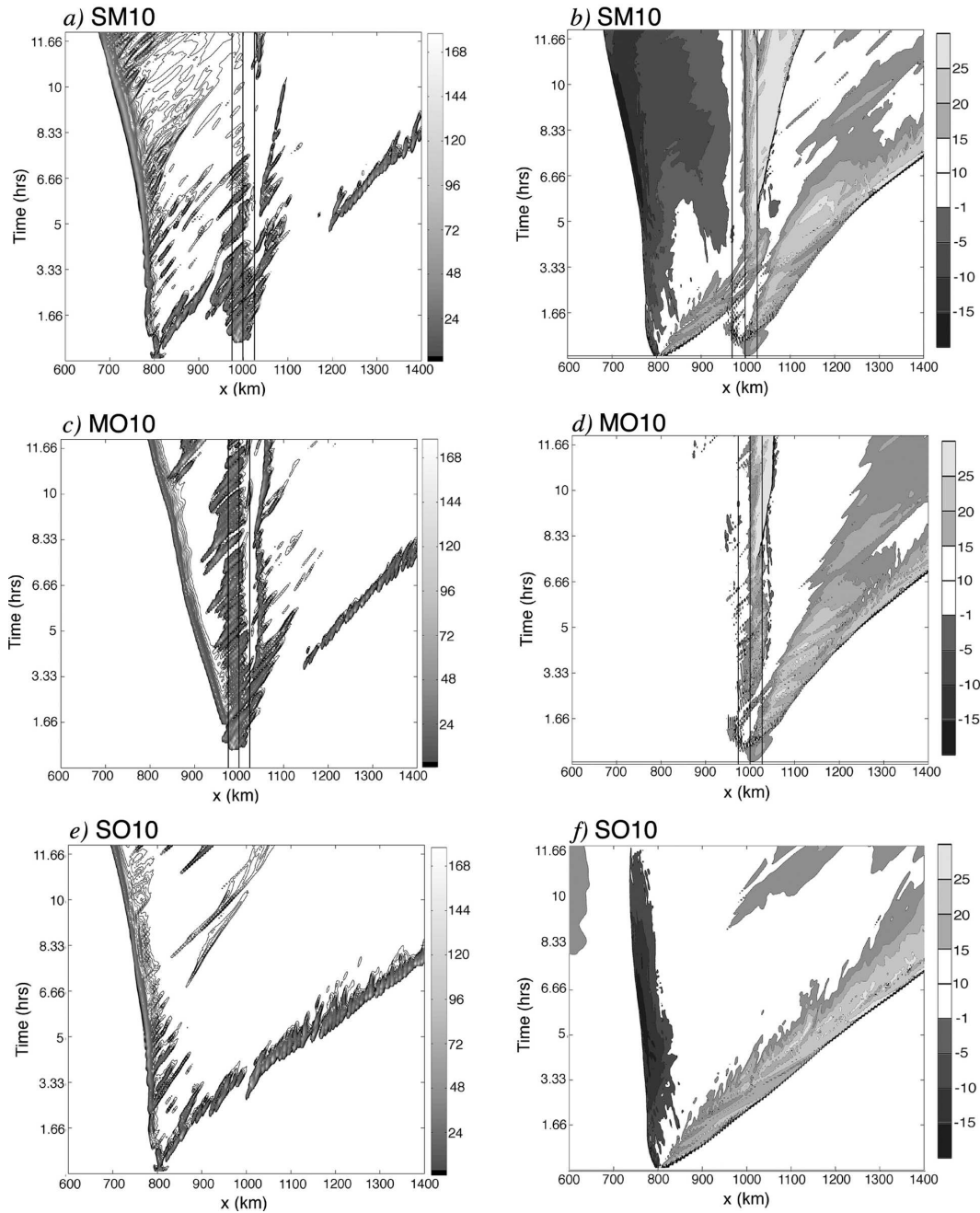


FIG. 8. Hovmöller diagrams of the rain rate for the (a) SM10, (c) MO10, and (e) SO10 simulations and Hovmöller diagrams of surface  $u$  winds for the (b) SM10, (d) MO10, and (f) SO10 simulations. The thin black lines in (a)–(d) denote the mountain peak and half-width.

tion of the flow fields in the MO15 and SO15 simulations.

Figure 11 provides an additional perspective of the flow and nonlinear interaction of the triggered and mountain-induced convective systems in the SM15 simulation. This figure shows  $\theta' < 0$  K and wind vectors. At  $t = 4$  h (Fig. 11a), the leading edge of the

density current (indicated by the thick arrow beneath each panel) was located at about  $x = 750$  km. Comparison of this figure with Fig. 2c shows that the density current, identifiable as the region of  $\theta' < -4$  K, in the SM15 simulation was marginally deeper than that in the SO15 simulation and did not extend as far downstream as that in the SO15 simulation. Figure 11b shows the

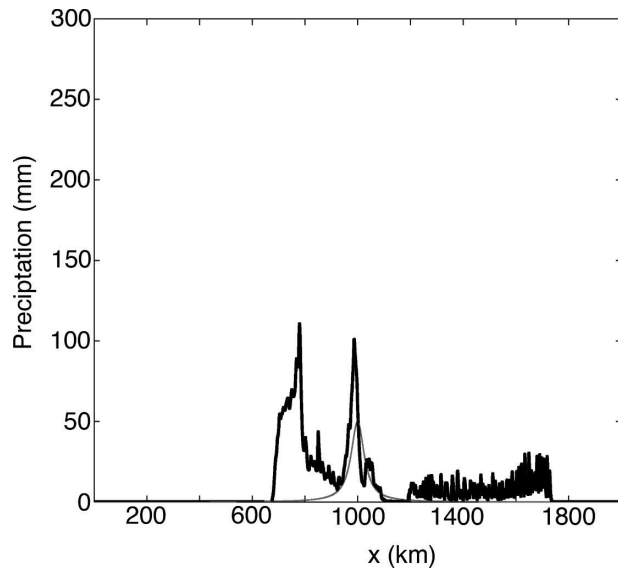


FIG. 9. The 12-h accumulated precipitation for the SM10 simulation.

same fields at  $t = 10$  h. There was a shallow density current upstream of the mountain whose leading edge was located at about  $x = 900$  km.

The accumulated precipitation for the SM15 simulation (Fig. 12) has a maximum of about 140 mm over the upslope of the mountain and a secondary maximum of 100 mm located about 90 km upstream of the mountain peak. Note that the maxima over the mountain peak in the SM10 and SM15 simulations were about 100 mm less than in their MO counterparts.

The nonlinear interaction, as we have dubbed it, leads to two important questions: What happens mechanically or dynamically when the two convective systems collide that ultimately causes the conjoined system to stagnate? Under what circumstances are similar results expectable in other atmospheric flows? Or, more precisely, are our results dependent on the mountain or sounding characteristics? These questions are explored in the following two sections.

#### 4. Dynamics leading to squall-line stagnation

Figure 13 shows a skew  $T$ - $\log p$  diagram of temperature and moisture from the SM15 simulation at  $t = 3$  h and  $x = 850$  km. This location is within the cooled region noted in Fig. 11. The Brunt-Väisälä frequency ( $N$ ) averaged from the surface to  $z = 2000$  m was compared for this sounding and that in Fig. 1a and found to be 0.013 and  $0.008 \text{ s}^{-1}$ , respectively. This increase in  $N$  resulted in a decrease in  $F$  from 0.95 to 0.63. Note that the latter value for  $F$  is less than the critical  $F$  (i.e., the

value of  $F$  for which the flow transitions from a blocked to an unblocked flow) for our MO simulations. Such a decrease in  $F$  is indicative that there was a flow regime shift in the SM15 simulation from an unblocked, linear-type flow to a blocked, nonlinear-type flow.

Figures 14a,b show the  $y$  vorticity for the SM15 simulation at  $t = 1$  and 5 h. Note the sign of the vorticity in Fig. 14 is consistent with a coordinate system that is right handed. In Fig. 14a, the left and right density currents associated with the triggered convective system are evident as the couplet of positive and negative vorticity centered at  $x = 800$  km. Aside from the convection-induced vorticity couplet, the mountain upslope was mostly characterized by vorticity values close to  $0 \text{ s}^{-1}$ . Over the mountain peak were narrow cells of positive and negative vorticity associated with the orographically induced convective system. By  $t = 5$  h (Fig. 14b), the right density current had passed over the mountain and the left density current was couched against the mountain upslope. Within this zone of positive vorticity were cores of vorticity in excess of  $0.03 \text{ s}^{-1}$ . For the sake of comparison, the vorticity distributions for the MO15 and MO5 simulations are provided in Figs. 14c,d, respectively. The  $y$  vorticity in the MO15 simulation (Fig. 14c) is fairly similar to that in Fig. 14a, except for the obvious difference that there was not a positive-negative couplet upstream of the mountain in the MO15 simulation. Otherwise, the flow along the mountain upslope had near-zero vorticity and there were cells of positive and negative vorticity over the mountain peak associated with the mountain-induced convection. Although the  $y$ -vorticity distribution in the MO5 simulation (Fig. 14d) is far from identical to that in the Fig. 14b, the MO5 and SM15 simulations at the times shown do have several commonalities. In particular, in both Figs. 14b,d, there is a zone of strong, positive vorticity nestled against the mountain upslope. This zone of positive vorticity is associated with the return flow that developed upstream of the mountain in each of these simulations, consistent with that in a blocked, nonlinear-type flow.

The dynamical cause of the flow regime shift in the SM15 simulation appears to be evaporative cooling since there were no other diabatic processes active in our simulations that could have caused such strong cooling. To test this notion, an experiment identical to the SM15 simulation, only with the thermal effects of evaporation deactivated (the neSM15 simulation) was performed. Precipitation was allowed in this simulation to prevent an unreasonably large orographic cloud from forming.

Figure 15a shows a vertical cross section of  $\theta'$ ,  $q_c$ , and wind vectors from the neSM15 simulation at  $t = 4$  h for

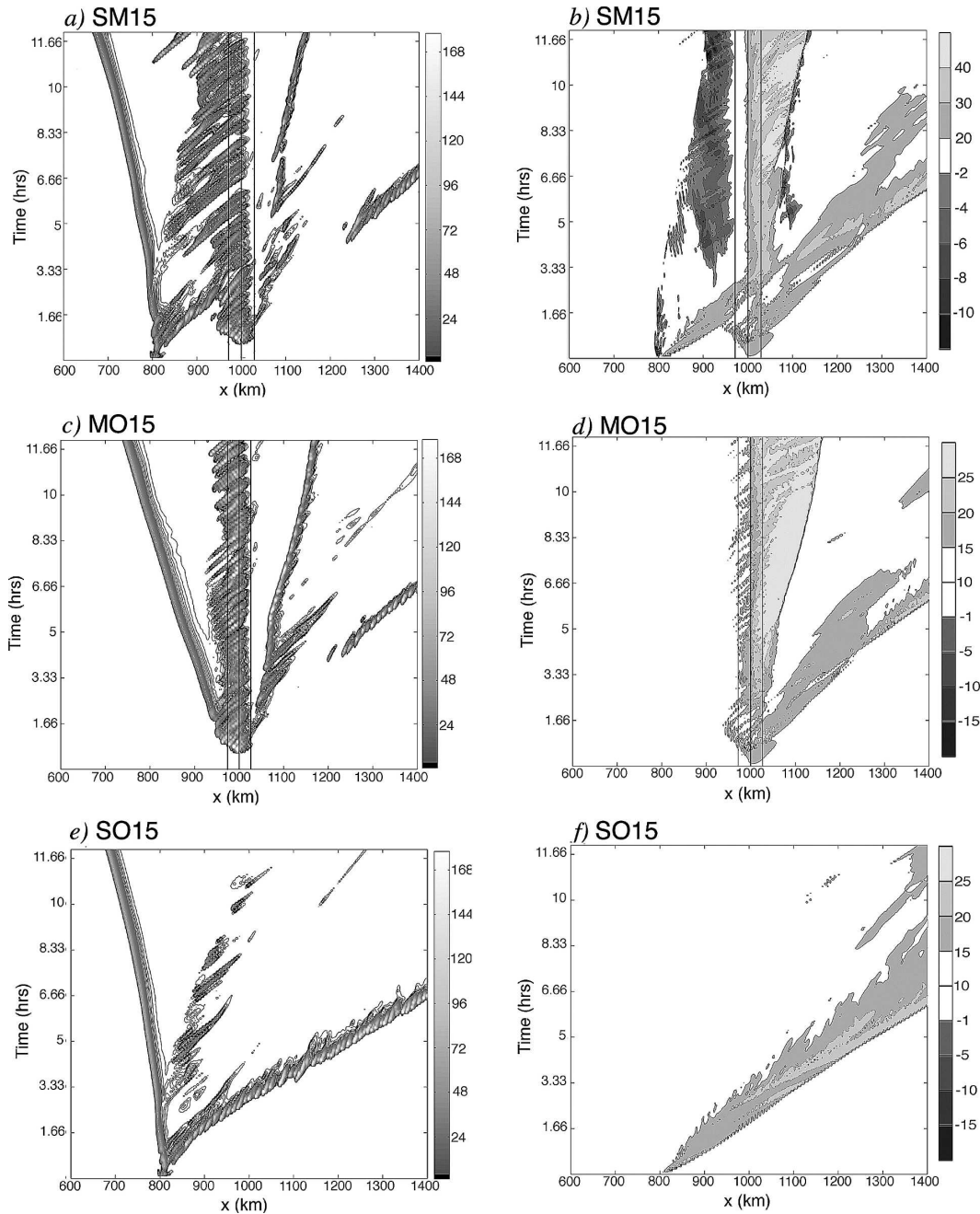


FIG. 10. Hovmöller diagrams of the rain rate for the (a) SM15, (c) MO15, and (e) SO15 simulations and Hovmöller diagrams of surface  $u$  winds for the (b) SM15, (d) MO15, and (f) SO15 simulations. The thin black lines in (a)–(d) denote the mountain peak and half-width.

the neSM15 simulation. The pronounced cool layer upstream of the mountain noted in the SM15 simulation (Fig. 11) was not present in the neSM15 simulation. Furthermore, the strongest vertical motions and convective activities were along the upslopes of the mountain in the neSM15 simulation rather than far upstream of the mountain. Hovmöller diagrams of the rain rate

and surface  $u$  winds for the neSM15 simulation are shown in Figs. 15b,c, respectively. A stationary precipitation system is evident over the mountain peak in Fig. 15b as well as a downstream-moving precipitation system that originated at  $x = 800$  km. This downstream-moving precipitation system crossed the mountain and phased with a hydraulic jump-like feature to the lee of

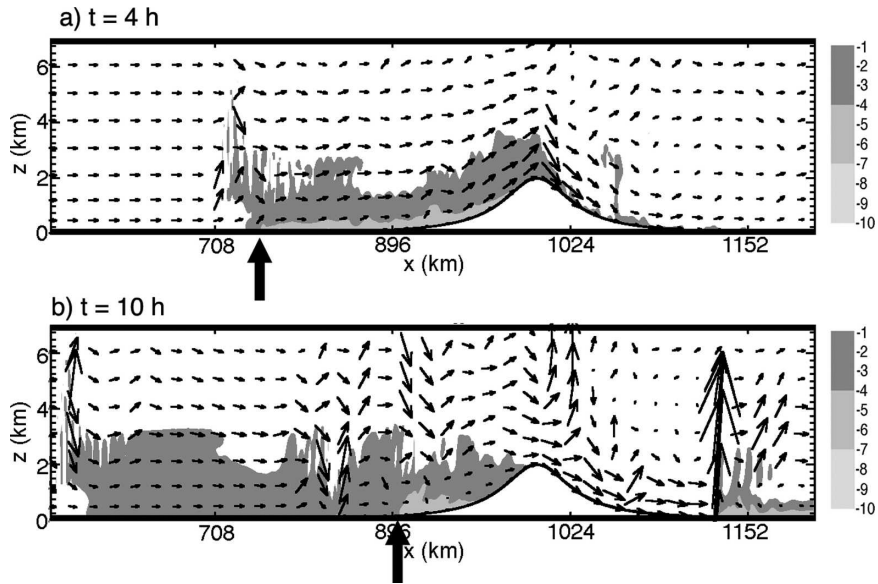


FIG. 11. Vertical cross section of perturbation potential temperature (shaded as in legend) and wind vectors for the SM15 simulation at  $t =$  (a) 4 and (b) 10 h. The thick arrows indicate the location of the leading edge of the left density current.

the mountain. Notice that a return flow did not develop upstream of the mountain in Fig. 15c as in the SM15 simulation (Fig. 10b). The 12-h accumulated precipitation (Fig. 15d) shows that the stationary precipitation system over the mountain peak was associated with a maximum of 226 mm. This maximum is close in magnitude to that over the mountain peak noted in the MO15 simulation (Fig. 5c). The downstream-propagating precipitation system that phased with the hydraulic jump to the lee of the mountain led to a secondary precipitation maximum of about

170 mm located roughly 250 km to the lee of the mountain.

**5. Sensitivity of results to initial conditions**

*a. Sensitivity to mountain height*

To test the sensitivity to mountain height, a set of experiments was performed wherein the mountain

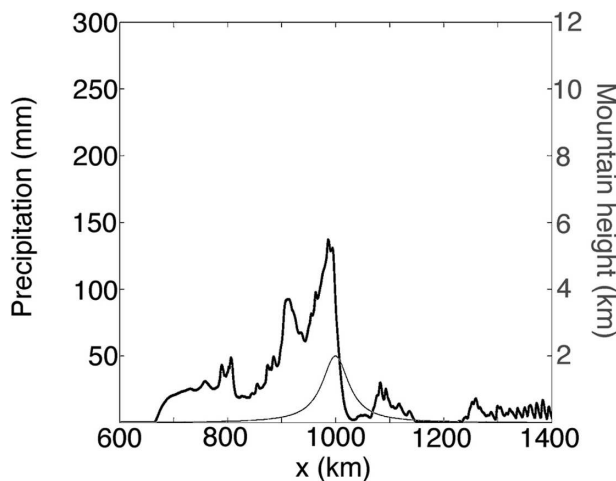


FIG. 12. The SM15 simulation output showing the 12-h accumulated precipitation.

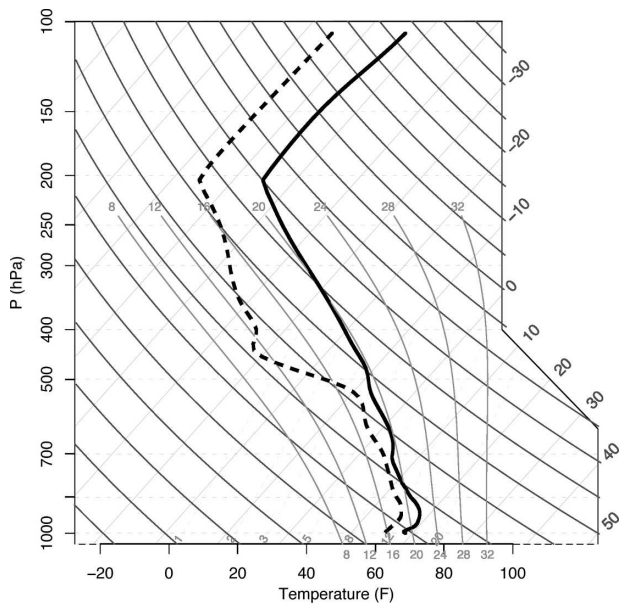


FIG. 13. Sounding taken from the SM15 simulation at  $t = 3$  h and  $x = 850$  km.

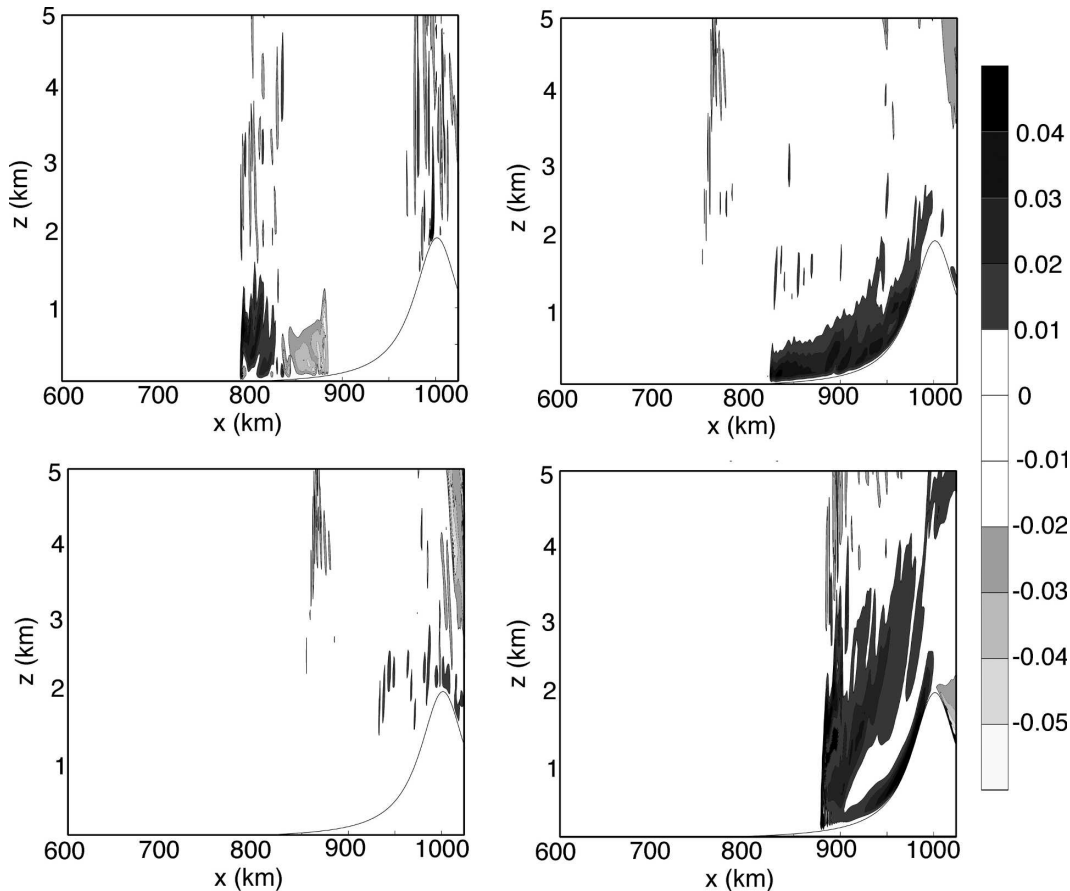


FIG. 14. The  $y$ -relative vorticity for the (top left) SM15 simulation at  $t = 1$  h, (top right) SM15 simulation at  $t = 5$  h, (bottom left) MO15 simulation at  $t = 5$  h, and (bottom right) MO5 simulation at  $t = 5$  h.

height was increased to 3 km. These simulations are otherwise identical to the MO and SM experiments and will be referred to as 3kmMO $X$  and 3kmSM $X$  where  $X$  refers to the basic-state wind speed,  $U$ .

Figure 16a shows a vertical cross section of  $\theta'$ ,  $q_c$ , and wind vectors at  $t = 10$  h for the 3kmMO5 simulation. As in the MO5 simulation, the 3kmMO5 case exhibited an upstream-propagating density current. This upstream-propagating density current was accompanied by an upstream-propagating precipitation system leading to a 12-h accumulated precipitation distribution (Fig. 16b) that is similar to that in the MO5 case. This simulation belongs to a blocked-type (or regime I) flow.

As in the blocked simulations with a 2-km-high mountain, squall-line stagnation did not occur for the blocked 3kmSM cases. This is demonstrated in Fig. 17a, which shows a Hovmöller diagram of the rain rate and surface  $u$  winds for the 3kmSM5 simulation. According to this figure, the mountain-induced and triggered convective systems propagated upstream merging at about  $t = 7$  h and  $x = 500$  km. Rain rates increased at the time

of the merger, however, the precipitation system continued to propagate upstream. Figure 17b shows the 12-h accumulated precipitation for the 3kmSM5 simulation. Although there are three distinct maxima upstream of the mountain peak in this figure, they are each only about 75 mm in magnitude.

Figure 18a shows the vertical cross section from the 3kmMO10 simulation at  $t = 10$  h. At this time, the density current was located just to the lee of the mountain peak. Inspection of other output times (not shown) indicates this density current remained quasi-stationary, consistent with a regime-II flow. Note that the flow regime transition occurred for a  $U$  wind speed of  $10 \text{ m s}^{-1}$  in the simulations with a 2-km-high mountain as well (Fig. 4b). Out of curiosity, another series of simulations was performed identical to the MO and SO simulations only with the mountain height reduced to 1 km. As in the other two sets of experiments, the transition from a blocked regime to an unblocked regime took place at a  $U$  wind speed of  $10 \text{ m s}^{-1}$  (not shown). According to Fig. 18b, the left density current in the 3

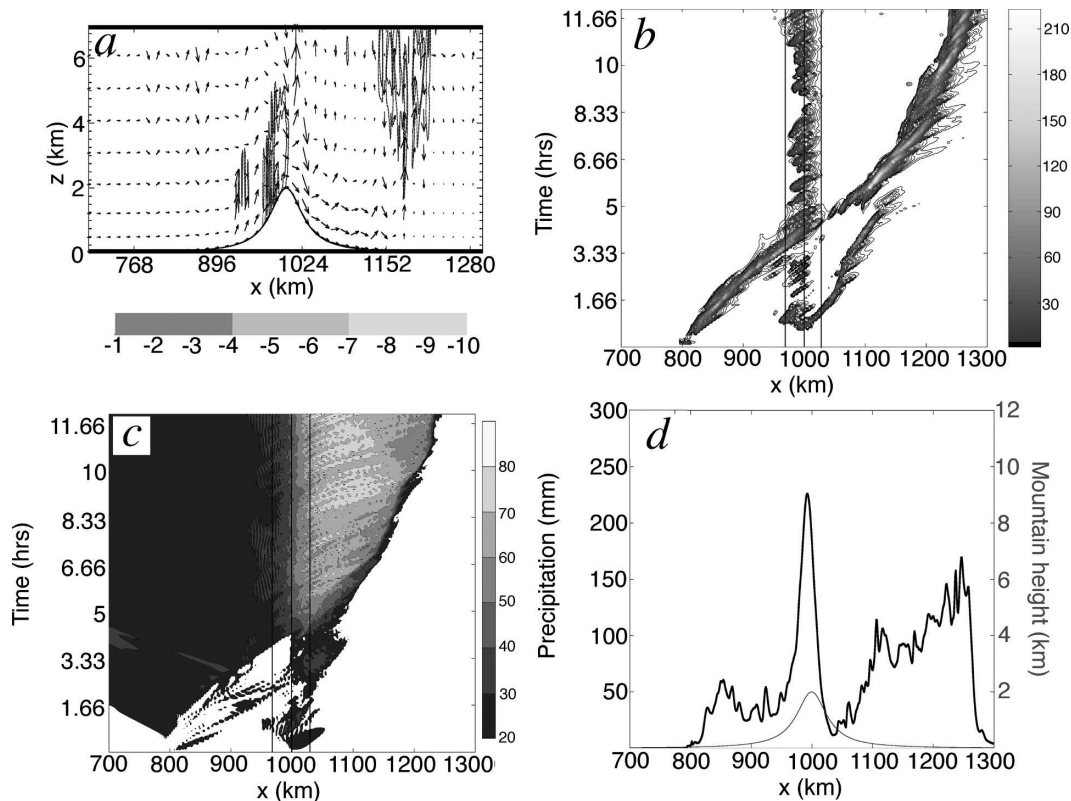


FIG. 15. The neSM15 simulation output showing (a) vertical cross section of perturbation potential temperature (shaded as in legend), cloud water mixing ratio (dotted contours; contoured every  $0.5 \text{ g kg}^{-1}$ ), and wind vectors for the neSM5 simulation at  $t = 4 \text{ h}$ ; (b) Hovmöller diagram of the rain rate; (c) Hovmöller diagram of surface  $u$  winds; and (d) the 12-h accumulated precipitation. The thin, black lines in (b) and (c) denote the mountain peak and half-width.

kmMO15 simulation propagated downstream. Notice that at the time shown in this figure, the left density current was positioned about 90 km downstream of the mountain peak. Hence, the 3 kmMO15 simulation belongs to regime III. The 12-h accumulated precipitation for the 3kmMO10 and 3 kmMO15 simulations is shown in Figs. 18c,d. As in the MO simulations, the maximum precipitation over the mountain peak increased with increasing  $U$  in the 3 kmMO simulations. In the 3kmMO10 (3kmMO15) simulation, the maximum was 335 (415) mm.

The Hovmöller diagrams of surface  $u$  winds and rain rate for the 3kmSM15 simulation are shown in Figs. 19a,b, respectively. A region of return flow is evident upstream of the mountain in Fig. 19a. Along the leading edge of the return flow was a stationary precipitation system (Fig. 19b). The 12-h accumulated precipitation (Fig. 19c) has a maximum over the mountain peak of about 180 mm. There is an even larger maximum of 200 mm located at  $x = 830 \text{ km}$  associated with the quasi-stationary precipitation system.

The above results are consistent with the simulations

performed using a 2-km-high mountain and indicate that our results are not due to the unique combination of  $N$  and  $h$ . However, a cautionary note is appropriate at this juncture: we have deliberately chosen mountain heights that are above the level of free convection for our sounding. The use of lower mountain heights may not yield a mountain-induced convective system (e.g., Frame and Markowski 2006) thereby disabling the nonlinear interactions that were so pivotal in causing the squall lines to become stationary in the higher  $F$  cases.

#### b. Sensitivity to choice of initial temperature and moisture stratification

Another set of experiments was performed using the initial temperature and moisture stratification shown in Fig. 20. This sounding, which is the observed sounding from Fort Sill, Oklahoma, on 20 May 1977 (Alderman and Droegemeier 2005, and citations therein), has an  $N$  of  $0.005 \text{ s}^{-1}$ . The mountain and triggered convective system characteristics are identical to those in Fig. 1b. The nomenclature for these simulations is as follows: mayMOX (maySMX) refers to the simulations with a

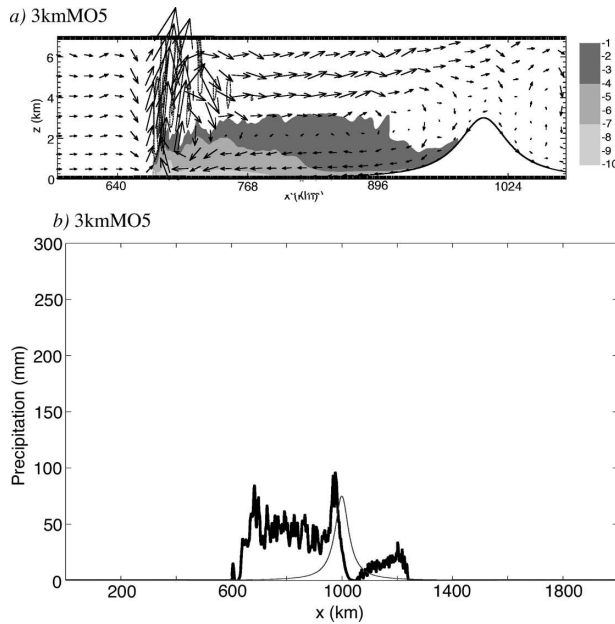


FIG. 16. The 3kmMO5 simulation output showing (a) vertical cross section of perturbation potential temperature (shaded as in legend), cloud water mixing ratio (dotted contours; contoured every  $0.5 \text{ g kg}^{-1}$ ), and wind vectors at  $t = 10 \text{ h}$ ; and (b) the 12-h accumulated precipitation.

mountain only (squall line and mountain) where the  $X$  is the basic-state wind speed. For the sake of brevity, the simulations with a squall line only will not be discussed as the results from these simulations add little to the overall scientific aim of this work.

Figure 21a shows a Hovmöller diagram of surface  $u$  winds for the mayMO5 case. The Froude number for this case is 0.51. Notice there existed an upstream-propagating density current, identifiable by the region of negative  $u$ . Lifting along the leading edge of this density current was responsible for the triggering of a precipitation system (Fig. 21c). There was also enhanced precipitation over the mountain peak. The 12-h accumulated precipitation (Fig. 21e) shows there was a maximum between 80 and 100 mm located over the mountain upslope. This maximum was associated with the stationary precipitation over the mountain upslope noted in Fig. 21c.

In the maySM5 case, the density currents associated with the triggered convective system and the mountain-induced convective system both propagated upstream throughout the integration period (Fig. 21b). The precipitation systems associated with these features also experienced a continuous upstream propagation and did not become stationary (Fig. 21d). The 12-h accumulated precipitation for the may SM5 simulation (Fig. 21f) indicates there was a more-or-less even distribution of rainfall upstream of the mountain.

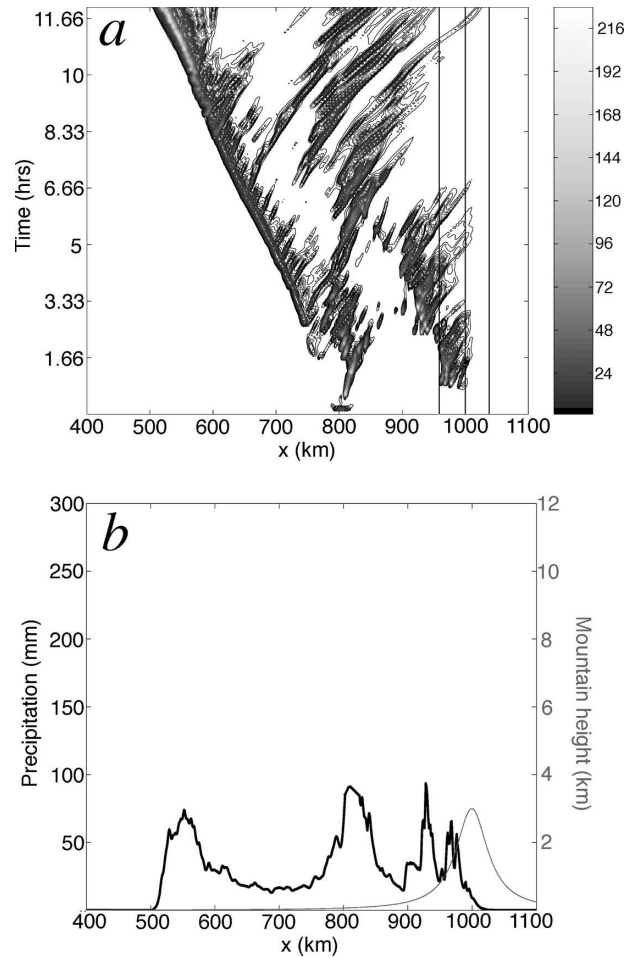


FIG. 17. The 12-h accumulated precipitation for the SM15 simulation, and the 3kmSM5 simulation output showing (a) Hovmöller diagram of the rain rate and (b) the 12-h accumulated precipitation. The thin, black lines in (a) denote the mountain peak and half-width.

The Hovmöller diagram of surface  $u$  winds for the mayMO15 case, which has an  $F$  of 1.53, is provided in Fig. 22a. Consistent with a linear, or flow-over, regime, there were strong downslope winds to the lee of the mountain. Also consistent with a linear flow, was the presence of a stationary precipitation system over the mountain peak and upslope (Fig. 22c) that led to a 12-h maximum in rainfall over the mountain peak of approximately 180 mm (Fig. 22e). In the maySM15 simulation, a region of negative  $u$  winds formed upstream of the mountain at about  $t = 5 \text{ h}$  (Fig. 22b). Note that the triggered convective system remained approximately stationary at about  $x = 800 \text{ km}$  throughout the integration period (Fig. 22d). Precipitation was also enhanced over the mountain peak itself. This led to a precipitation maximum at about  $x = 800 \text{ km}$  of about 180 mm

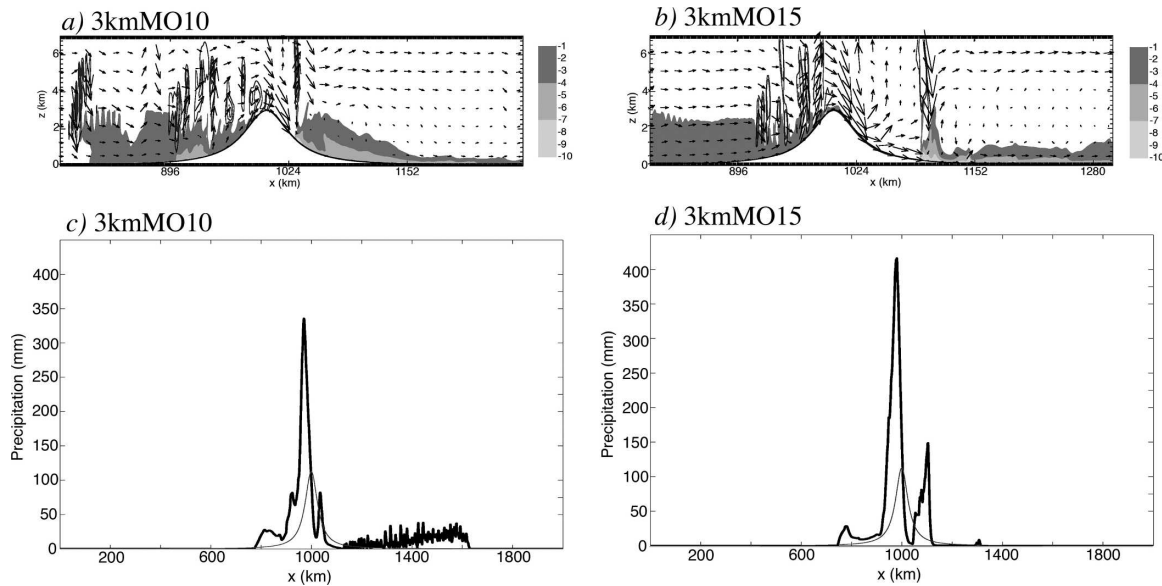


FIG. 18. Vertical cross sections of perturbation potential temperature (shaded as in legend), cloud water mixing ratio (dotted contours; contoured every  $0.5 \text{ g kg}^{-1}$ ), and wind vectors at  $t = 10$  h for the (a) 3kmMO10 and (b) 3 kmMO15 simulations, and the 12-h accumulated precipitation for the (c) 3kmMO10 and (d) 3 kmMO15 simulations.

and a secondary maximum at  $x = 1000$  km of 80 mm (Fig. 22f).

The flow patterns in the above set of simulations are by no means identical to those obtained using the Weismann-Klemp sounding (Fig. 1a). However, similar phenomena did occur suggesting that the results have generality to other conditionally unstable flows impinging on a mountain. But again, a cautionary note is apropos. We have intentionally chosen a sounding that is both conditionally unstable (for obvious reasons since this is the type of flow this paper is concerned with) and is not saturated in the lowest layers. If the surface layer of air were saturated, squall-line stagnation would not likely occur since evaporative cooling could not act to alter the thermodynamic characteristics of airstreams immediately upstream of the mountain as was discussed in section 4.

### c. Sensitivity to the choice of surface cold perturbation

The sensitivity of the results on the choice of a surface cold perturbation was tested by performing a simulation identical to the SO10 simulation only with the convection triggered by an elevated warm bubble that was 2 K warmer than the environment, the bubSO10 simulation. This warm bubble was positioned so that its center was 2 km above ground level. Its radius in the  $x$  ( $z$ ) direction was 5 km (1.4 km). Figure 23a shows a Hovmöller diagram of the rain rate for the bubSO10

simulation. Note that in both the SO10 simulation (Fig. 8e) and the bubSO10 simulation, there was a stationary precipitation system at  $x = 800$  km. The only major difference between Figs. 23a and 8e is that between  $t = 0$  and 1.5 h, the triggered convective system in the bubSO10 simulation moved downstream whereas in the SO10 simulation, it remained stationary. According to Fig. 23b, which shows the bubSO10 Hovmöller diagram of surface  $u$  winds, a region of return flow originating at  $x = 800$  km developed at about  $t = 1$  h. In the SO10 case (Fig. 8f), a return flow was present starting just after  $t = 0$  h. This difference likely accounts for the downstream advection of the convective system in the bubSO10 simulation during the first 1.5 h of integration. Note that the leading edge of the return flow after  $t = 2$  h in Fig. 16b was similarly located and of similar strength to that in the SO10 simulation.

## 6. Discussion and conclusions

The effects of a mountain on the propagation and precipitation distribution of a preexisting convective systems for different Froude number flow regimes was examined through a series of two-dimensional, idealized simulations. The simulations included three sets of experiments: the SO simulations, which had a convective system triggered by a cold pool but no mountain; the MO simulations, which had a mountain, but no cold

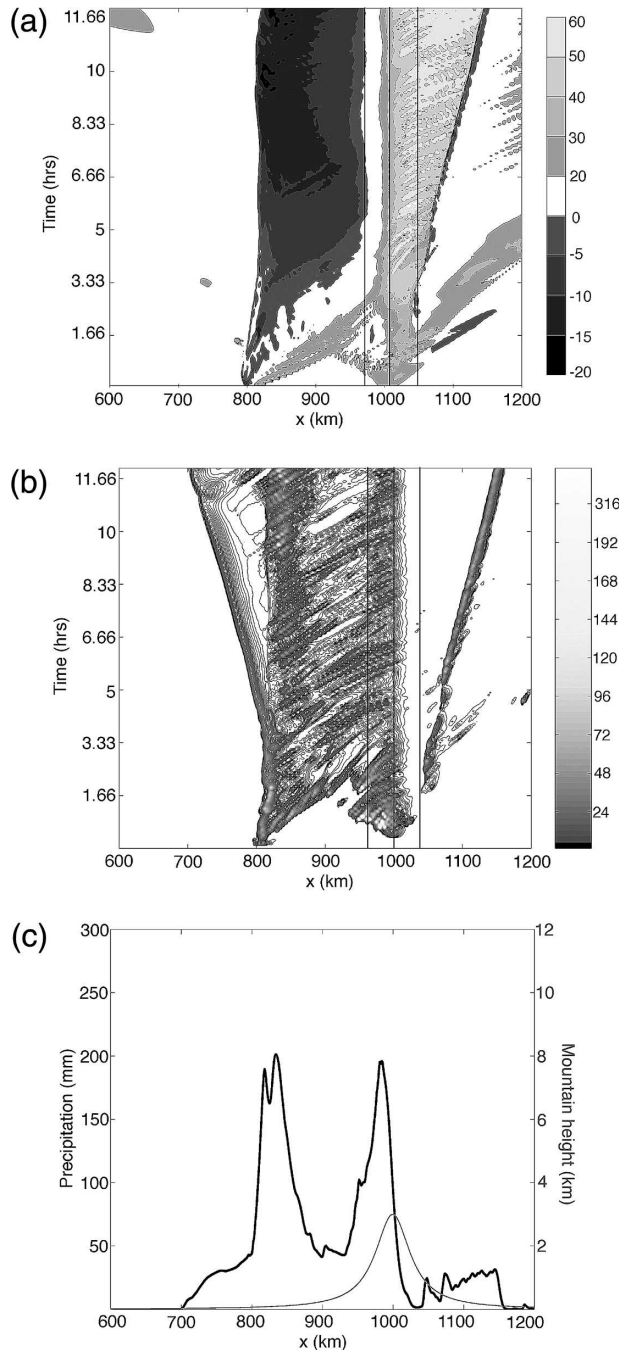


FIG. 19. The 3kmSM15 simulation output showing (a) Hovmöller diagram of surface  $u$  winds, (b) Hovmöller diagrams of the rain rate, and (c) the 12-h accumulated precipitation. The thin, black lines in (a) and (b) denote the mountain peak and half-width.

pool-triggered convective system; and the SM experiments, which had both a mountain and a convective system triggered by a cold pool.

It was noted that for  $U$  wind speeds less than 10

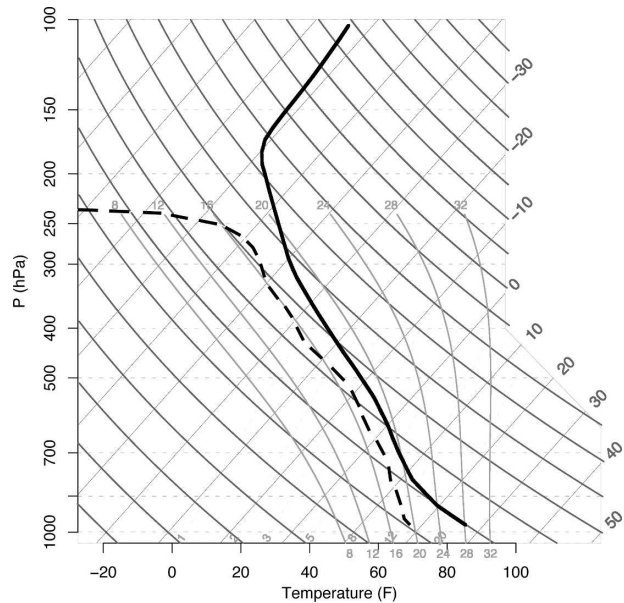


FIG. 20. Observed sounding from Ft. Sill, OK, on 20 May 1977.

$\text{m s}^{-1}$ , the flow was in a blocked regime and the left convection-induced density current propagated upstream in both the MO and SO simulations. When a convective system was triggered upstream of the mountain in the SM simulations with  $U < 10 \text{ m s}^{-1}$ , the density currents associated with the mountain and the triggered convective system propagated upstream and did not become stationary. For  $U$  wind speeds greater than  $10 \text{ m s}^{-1}$ , the flow was in an unblocked, or linear regime and both convection-induced density currents were swept downstream by the relatively strong basic-state wind. There was also a stationary precipitation system over the mountain peak and upslope in these simulations. In the unblocked SM simulations, there was a stationary precipitation system located between 100 and 200 km upstream of the mountain peak. This result suggests that squall-line stagnation is more prone to occur for relatively higher  $F$  flows.

The dynamics responsible for the precipitation distribution and squall-line motion in the SM15 simulation were explored. It was found that that evaporative cooling immediately upstream of the mountain acted to shift the flow into a low  $F$  or blocked flow regime. It was also noted that although the flow in the SO15 and MO15 simulations was linear, the interaction of the triggered and mountain-induced convective systems in the SM15 simulation was nonlinear.

A series of simulations were performed to insure the generality of our results to other conditionally unstable flows impinging on a mesoscale mountain. In the first set of experiments, the mountain height was increased

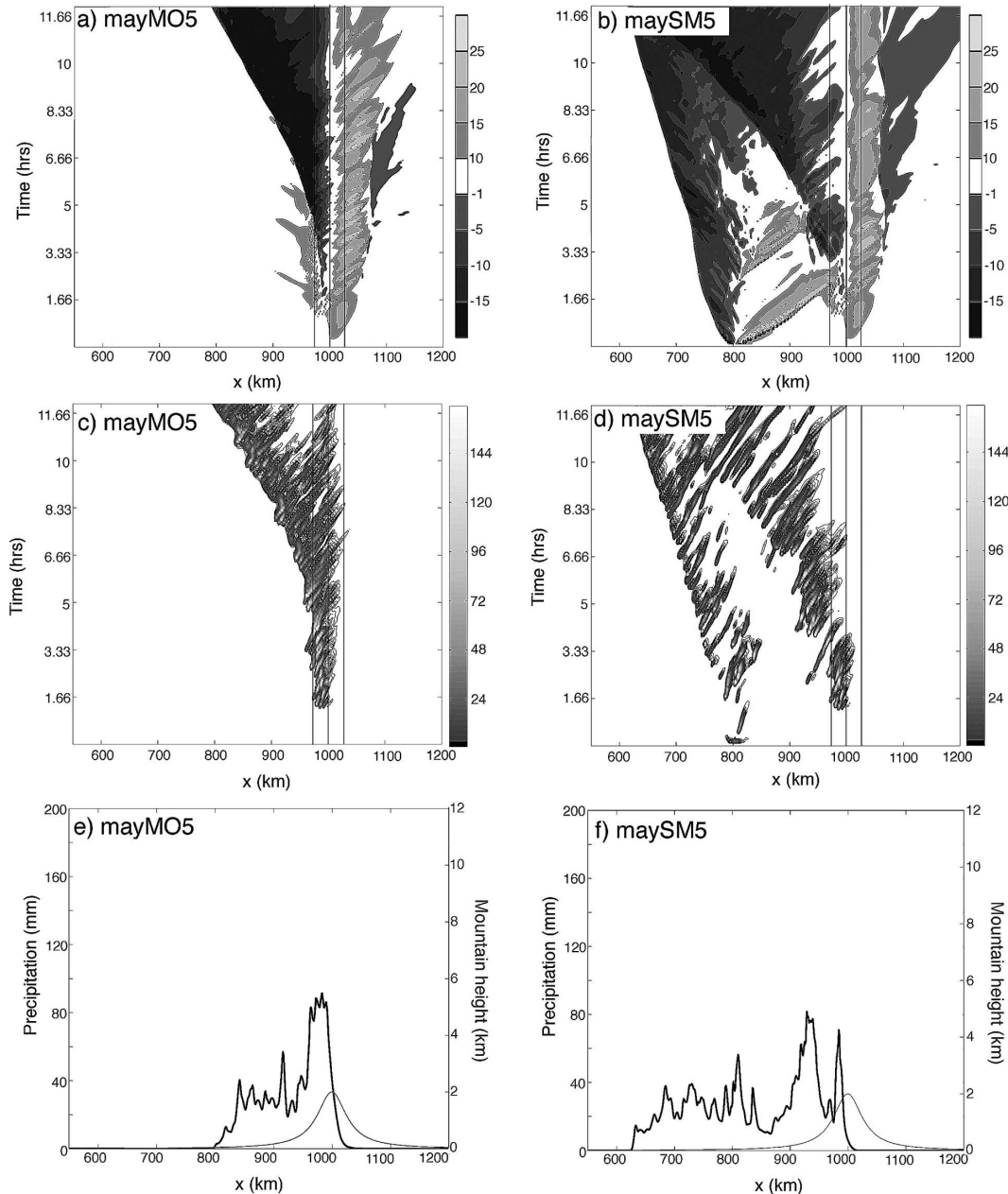


FIG. 21. Hovmöller diagram of surface  $u$  winds for the (a) mayMO5 and (b) maySM5 cases. Hovmöller diagram of the rain rate for the (c) mayMO5 and (d) maySM5 cases. The 12-h accumulated precipitation for the (e) mayMO5 and (f) maySM5 cases. The thin black lines in (a)–(d) denote the mountain peak and half-width.

(decreased) to 3 (1) km. These experiments yielded an unexpected result, namely that the  $U$  wind speed for which the transition from the blocked to the unblocked flow regime occurred was the same as that for the 2-km simulations,  $10 \text{ m s}^{-1}$ . A comparison of the Froude number at which this transition occurs indicates that the critical Froude numbers are 0.42, 0.69, and 0.73 for the 1-, 2-, and 3-km simulations, respectively. This suggests

that flow regime transition for moist, conditionally unstable flow over a mountain is not necessarily dependent on the mountain characteristics. However, additional testing is required to better understand the physical mechanisms responsible for blocking of moist, conditionally unstable flow. More importantly, though, the 3- and 1-km simulations exhibited behavior that was very similar to the 2-km simulations. Hence, our results

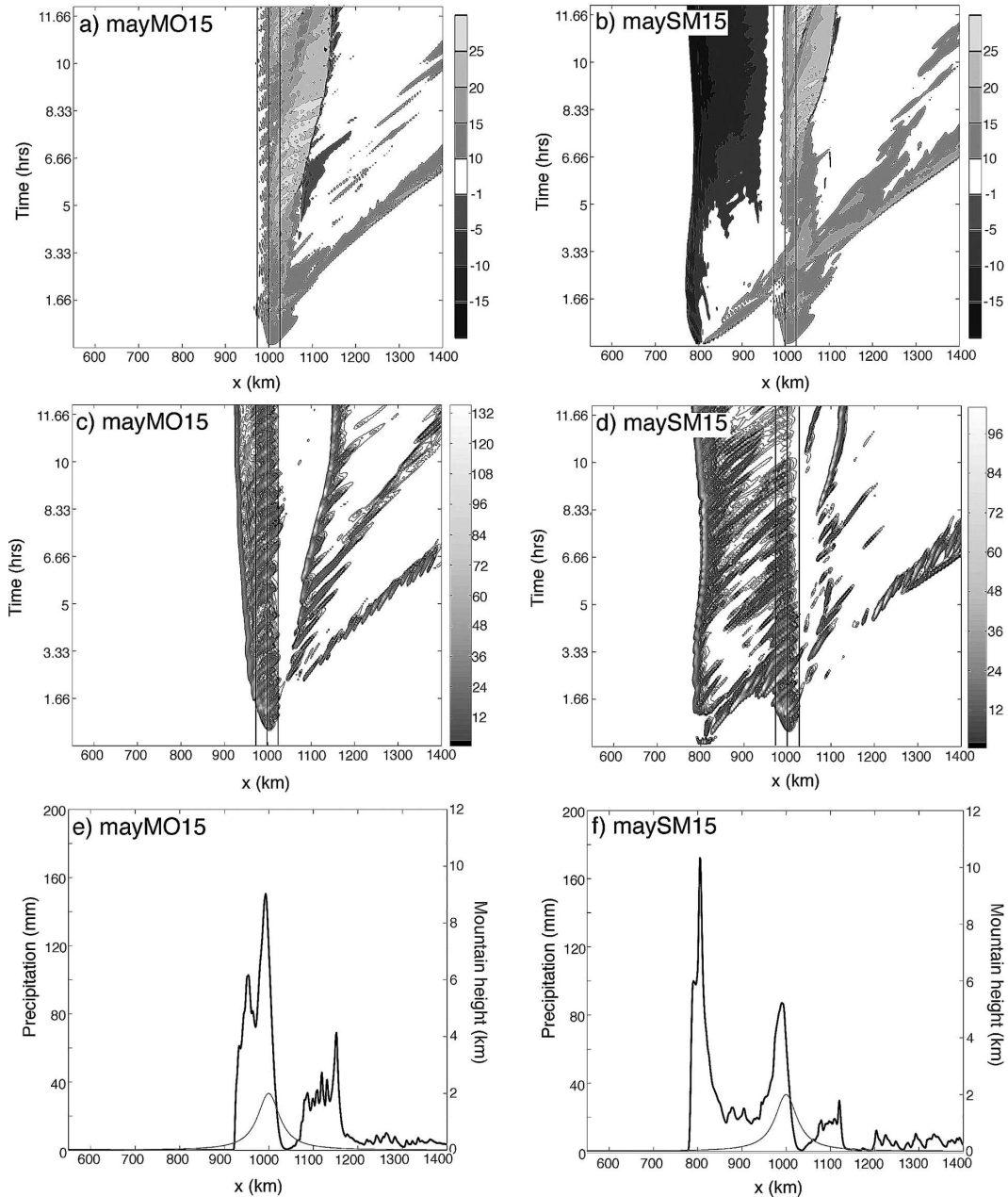


FIG. 22. Hovmöller diagram of surface  $u$  winds for the (a) mayMO15 and (b) maySM15 cases. Hovmöller diagram of the rain rate for the (c) mayMO15 and (d) maySM15 cases. The 12-h accumulated precipitation for the (e) mayMO15 and (f) maySM15 cases. The thin black lines in (a)–(d) denote the mountain peak and half-width.

do not appear to be dependent on the choice of mountain height.

A final series of simulations were performed using a different initial temperature and moisture profile. As in all other sets of experiments, squall-line stagnation did not occur for the low  $F$  flows. Rather, it was in the high  $F$  flows that a stationary precipitation system formed upstream of the mountain. These findings suggest our

results have generality to other conditionally unstable flows impinging on a mountain, assuming the predominant mechanism (i.e., evaporative cooling) is active. However, there are two caveats to our findings of importance. The first is that our results are dependent on the mountain being high enough so that air parcels impinging on the mountain reach their levels of free convection. If the mountain is not sufficient to generate

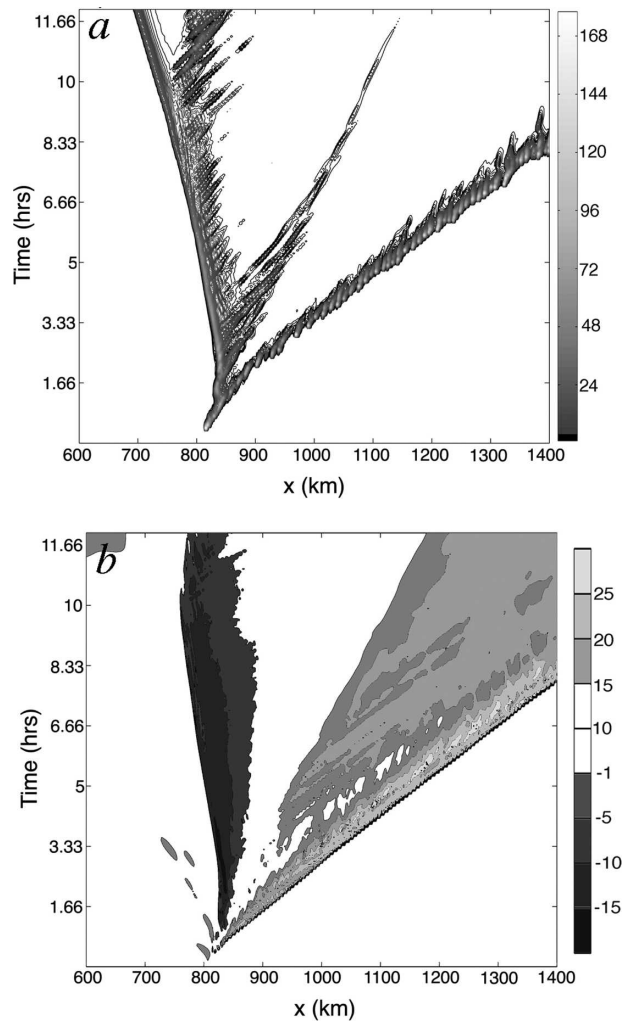


FIG. 23. Hovmöller diagrams of the (a) rain rate and (b) surface  $u$  winds for the bubSO10 simulation.

convection, the nonlinear interaction noted in the SM15 simulation will not occur and stagnation may not be observed (e.g., Frame and Markowski 2006). The second is that the low-level air must be subsaturated in order for significant evaporation to occur.

The investigation of what happens when a preexisting convective system impinges on a mountain is still in its infancy and similar results may not be obtained for thermodynamic profiles that are not conditionally unstable. Moreover, there are several processes not examined herein that could affect the motion of a squall line as it impinges on a mountain including diurnal heating (Chen et al. 1991), frontal circulations (Chen and Chi 1978), and changes in surface roughness (Kirshbaum and Durran 2005). Future research is recommended to assess how these forcings affect squall-line motion in the presence of a mountain.

**Acknowledgments.** The authors wish to acknowledge R. Rotunno, G. Janowitz, F. Semazzi, M. Kaplan, PAMS HPC, CAPS, and NSF Grant ATM-0344237.

#### REFERENCES

- Akaeda, K., J. Reisner, and D. Parsons, 1995: The role of meso-scale and topographically induced circulations in initiating a flash flood observed during the TAMEX project. *Mon. Wea. Rev.*, **123**, 1720–1739.
- Alderman, E. J., and K. K. Droegemeier, 2005: The dependence of numerically simulated cyclic mesocyclogenesis upon environmental vertical wind shear. *Mon. Wea. Rev.*, **133**, 3593–3623.
- Britter, R. E., and J. E. Simpson, 1980: A laboratory model of an atmospheric mesofront. *Quart. J. Roy. Meteor. Soc.*, **106**, 485–500.
- Caracena, F., R. A. Maddox, L. R. Hoxit, and C. F. Chappell, 1979: Mesoanalysis of the Big Thompson storm. *Mon. Wea. Rev.*, **107**, 1–17.
- Chen, C.-S., W.-S. Chen, and Z. Deng, 1991: A study of a mountain-generated precipitation system in northern Taiwan during TAMEX IOP 8. *Mon. Wea. Rev.*, **119**, 2574–2607.
- Chen, G. J.-T., and S. S. Chi, 1978: On the meso-scale structure of Mei-Yu front in Taiwan (in Chinese with English abstract). *Atmos. Sci.*, **5**, 35–47.
- , and H. C. Chou, 1993: General characteristics of squall lines observed in TAMEX. *Mon. Wea. Rev.*, **121**, 726–733.
- Chen, S.-H., and Y.-L. Lin, 2000: Effects of orography on the generation and propagation of mesoscale convective systems in a two-dimensional conditionally unstable flow. *J. Atmos. Sci.*, **57**, 3817–3837.
- , and —, 2005a: Orographic effects on a conditionally unstable flow over an idealized three-dimensional mesoscale mountain. *Meteor. Atmos. Phys.*, **88**, 1–21.
- , and —, 2005b: Effects of moist Froude number and CAPE on a conditionally unstable flow over a mesoscale mountain. *J. Atmos. Sci.*, **62**, 331–350.
- Frame, J., and P. Markowski, 2006: The interaction of simulated squall lines with idealized mountain ridges. *Mon. Wea. Rev.*, **134**, 1919–1941.
- Galewsky, J., and A. Sobel, 2005: Moist dynamics and orographic precipitation in northern and central California during the New Year's flood of 1997. *Mon. Wea. Rev.*, **133**, 1594–1612.
- Jiang, Q., 2003: Moist dynamics and orographic precipitation. *Tellus*, **55A**, 301–316.
- Kirshbaum, D. J., and D. R. Durran, 2005: Observations and modeling of banded orographic convection. *J. Atmos. Sci.*, **62**, 1463–1479.
- Kuo, H.-C., and G. T.-J. Chen, 1990: The Taiwan Area Mesoscale Experiment (TAMEX): An overview. *Bull. Amer. Meteor. Soc.*, **71**, 488–503.
- Lin, Y.-L., R. D. Farley, and H. D. Orville, 1983: Bulk parameterization of the snow field in a cloud model. *J. Climate Appl. Meteor.*, **22**, 40–63.
- Liu, C., and M. W. Moncrieff, 1996: An analytical study of density currents in sheared, stratified fluids including the effects of latent heating. *J. Atmos. Sci.*, **53**, 3303–3312.
- Medina, S., and R. A. Houze, 2003: Air motions and precipitation growth in Alpine storms. *Quart. J. Roy. Meteor. Soc.*, **129**, 345–372.

- Miglietta, M. M., and A. Buzzi, 2004: A numerical study of moist stratified flow regimes over isolated topography. *Quart. J. Roy. Meteor. Soc.*, **130**, 1749–1770.
- Overland, J. E., and N. A. Bond, 1995: Observations and scale analysis of coastal wind jets. *Mon. Wea. Rev.*, **123**, 2934–2941.
- Raymond, D. J., and R. Rotunno, 1989: Response of a stably stratified flow to cooling. *J. Atmos. Sci.*, **46**, 2830–2837.
- Wang, J.-J., R. M. Rauber, H. T. Ochs III, and R. E. Carbone, 2000: The effects of the island of Hawaii on offshore rainband evolution. *Mon. Wea. Rev.*, **128**, 1052–1069.
- Weisman, M. L., and J. B. Klemp, 1982: The dependence of numerically simulated convective storms on vertical wind shear and buoyancy. *Mon. Wea. Rev.*, **110**, 504–520.
- Xue, M., and Coauthors, 2001: The advanced regional prediction system (ARPS)—A multiscale nonhydrostatic atmospheric simulation and prediction tool. Part II: Model physics and applications. *Meteor. Atmos. Phys.*, **76**, 134–165.